*minerals*

MDPI

*Article*

# Computed Tomography of Flake Graphite Ore: Data Acquisition and Image Processing

**Leonard T. Krebbers *, Bernd G. Lottermoser and Xinmeng Liu**

Institute of Mineral Resources Engineering, RWTH Aachen University, Wüllnerstraße 2, 52062 Aachen, Germany
* Correspondence: krebbers@mre.rwth-aachen.de

**Abstract:** A solid knowledge of the mineralogical properties (e.g., flake size, flake size distribution, purity, shape) of graphite ores is necessary because different graphite classes have different product uses. To date, these properties are commonly examined using well-established optical microscopy (OM), scanning electron microscopy with energy dispersive X-ray spectroscopy (SEM-EDS) and SEM-based automated image analysis. However, these 2D methods may be subject to sampling errors and stereological effects that can adversely affect the quality of the analysis. X-ray microcomputed tomography (CT) is a nondestructive imaging technique allowing for examination of the interior and exterior of solid materials such as rocks and ores in 3D. This study aimed to explore whether CT can provide additional mineralogical information for the characterisation of graphite ores. CT was used in combination with traditional techniques (XRD, SEM-EDS, OM) to examine a flake graphite ore in 3D. A scanning protocol for the examined graphite ore was established to acquire high-quality CT data. Quantitative mineralogical information on key properties of graphite was obtained by developing a deep learning-based image processing strategy. The results demonstrate that CT allows for the 3D visualisation of graphite ores and provides valid and reliable quantitative information on the quality-determining properties that currently cannot be obtained by other analytical tools. CT allows improved assessment of graphite deposits and their beneficiation.

**Keywords:** computed tomography; natural graphite; segmentation; ore analysis; machine learning; lithium-ion batteries

check for updates

**Citation:** Krebbers, L.T.; Lottermoser, B.G.; Liu, X. Computed Tomography of Flake Graphite Ore: Data Acquisition and Image Processing. *Minerals* **2023**, *13*, 247. https://doi.org/10.3390/min13020247

Academic Editors: Qinfu Liu, Kuo Li and Shuai Zhang

Received: 13 January 2023
Revised: 3 February 2023
Accepted: 6 February 2023
Published: 9 February 2023

**Copyright:** © 2023 by the authors. Licensee MDPI, Basel, Switzerland. This article is an open access article distributed under the terms and conditions of the Creative Commons Attribution (CC BY) license (https://creativecommons.org/licenses/by/4.0/).

## 1. Introduction

Natural graphite is an allotrope of carbon comprising a multitude of layers of graphene, i.e., one-atom thick, hexagonal lattice layer of carbon with carbon atoms connected to each other by covalent bonds [1]. The individual graphene layers are held together by van der Waals forces. These weak interplanar interactions endow the mineral graphite with exceptional properties such as refractoriness, high heat and electrical conductivity, greasiness and high thermal resistance [2]. Graphite is applied in a variety of technological applications including lithium-ion batteries (LIB), fuel cells, two-dimensional graphene electronics and fibre optics [2,3]. Consequently, natural graphite has been recognised as a critical raw material by mega economies such as the United States and the European Union because of its high economic importance and supply risk [4,5]. Today, China accounts for almost 75% of the global natural graphite production, followed by Mozambique and Brazil. Together, the three countries represent around 90% of the world's production [6].

Natural graphite is found in the Earth's crust in a variety of geological settings and results from the conversion of carbonaceous matter through metamorphic processes into graphite (graphitisation) or by deposition from carbon-bearing fluids [7,8]. There are various classification schemes, one of which divides graphite deposits according to their formation conditions into (1) lump (vein), (2) flake and (3) amorphous (microcrystalline) graphite [7]. In market terms, graphite is classified according to the particle (flake) size (Table 1). In contrast to many other mineral resources, the quality of graphite ore is

not solely determined predominantly based on grade, but rather on its mineralogical properties such as grain (flake) size, distribution, shape and purity. These properties are directly related to market applications and product price [9,10]. Graphite deposits that contain a high proportion of large graphite flakes tend to have higher purities and carbon content. The flake size distribution is deposit-specific and decisive for the economic viability of a deposit as well as the ultimate use of the concentrates produced [11]. To date, only graphite with high purity and large flake sizes can be used for LIB [12]. There are recent developments to use smaller flakes for LIB manufacturing. Regardless, rigorous characterisation of the raw material is key to assessing ore quality and achieving the best possible beneficiation product.

**Table 1.** Market terminology of natural graphite and general properties (modified after [10,13]).

| Classification | Size in µm | Carbon Content of Concentrates (%) |
|---|---|---|
| Amorphous | <75 | 75–90 |
| Small flake | 75–150 | 90–97 |
| Medium flake | 150–180 | 90–97 |
| Large flake | 180–300 | 90–97 |
| Jumbo | 300–500 | 90–97 |
| Super jumbo | >500 | 90–97 |

Graphite raw materials are conventionally characterised using X-ray powder diffraction (XRD), differential thermal analysis/thermogravimetry (DTA/TG), inductively coupled plasma mass spectrometry (ICP-MS), scanning electron microscopy coupled with an energy dispersive detector (SEM-EDS), Raman spectroscopy and optical microscopy (OM) as well as SEM-based automated mineralogy systems such as QEMSCAN (quantitative evaluation of minerals by scanning electron microscopy) and MLA (mineral liberation analyser), e.g., [14–17]. Results of these techniques provide vital information on the presence and properties of graphite ores. In some cases, the acquired information cannot be related to any dimensional geometries of the analysed samples (e.g., XRD). By contrast, OM, SEM-EDS, QEMSCAN and MLA allow for 2D visualisation of graphite ores. However, these techniques are time-consuming, and their sample preparation is destructive and requires careful sectioning of the original sample (e.g., drill hole) to select representative sample material. Moreover, results of the above-mentioned methods must be translated into the third dimension and are therefore subject to stereological bias [18]. For ores of complex mineralogy and microstructure such as graphite ores, where grain size distribution is an important assessment feature, this can be challenging. In view of the fact that graphite ores and deposits and their products represent 3D arrays of mineral assemblages, there is a need to acquire information on the 3D distribution of the quality-determining properties (i.e., flake size, intergrowth) of graphite in ores to achieve optimal processing and target use of graphite ores.

A novel tool to display the 3D distribution of mineral phases is X-ray microfocus computed tomography (CT). For example, several scientific studies have demonstrated the use of CT to define the in situ location of gold grains and their distribution within gold ores [19–22]. Ghorbani et al. successfully used CT for the 3D characterisation of crack and mineral dissemination in sphalerite ore particles [23]. Godel et al., Godel and Sittner et al. studied the 3D distribution of platin group metals (PGMs) to understand ore-forming processes [24–26]. Le Roux et al. quantified tungsten ore mineral content and ore grade using CT to assess the quality of the tungsten ore [27]. Similarly, Rozendaal et al. demonstrated the ability to quantify the final product quality grain size distribution, perform grain shape definition and identify external and internal mineral textures of a Ti-Zr placer deposit [28].

To date, however, the use of CT has not been comprehensively tested to characterise graphite raw materials. This study explores the application of CT for the characterisation of graphite ores. An image protocol was developed to acquire appropriate CT data. Fur-

thermore, an advanced image processing strategy was established that was based on deep learning algorithms to extract quantitative information on key microstructural features of the flake graphite ore in 3D. This study demonstrates that CT imaging of graphite ores requires careful development of image protocols and processing strategies, which can then produce new insights into graphite ore properties.

## 2. Materials and Methods

### *2.1. Conventional Mineralogical and Petrographic Analyses*

A flake graphite ore sample was provided by the German-based company NGS Trading & Consulting GmbH (Leinburg, Germany) from the Yanxin graphite mine (Shangdong province, China). XRD was carried out on a ~2.5 g aliquot of the sample, which was ground in 100% ethanol in a McCrone micronizing mill using synthetic agate pellets for 5 min. Micronized aliquots were air-dried and subsequently analysed on a Rigaku Ultima IV powder X-ray diffractometer (Department of Earth and Atmospheric Sciences, University of Alberta, Edmonton, Canada). The Rigaku Ultima IV XRD is equipped with a Co source that was operated at 38 kV and 38 mA. XRD patterns were collected from 5 to 80° 2q using a step size of 0.02° 2q at a rate of 1.2° 2q/minute. Qualitative phase identification was performed using the JADE (Rigaku, Tokyo, Japan) and EVA (Bruker, Billerica, MA, USA) software packages. Mineral phases were identified with reference to the International Center for Diffraction Data Powder Diffraction File 4+ database (ICDD PDF4+). For petrographic analysis, a thin section and cylindrical-shaped polished block were prepared by MK Factory (Stahnsdorf, Germany). Both samples were examined using a LEICA DM 2700P polarization microscope (Institute of Mineral Resource Engineering, RWTH Aachen University, Aachen, Germany). Microphotographs were taken with a LEICA FLEXCAM C1 camera to establish an image mosaic of the polished section using the LEICA LAS software. Scanning electron microscopy combined with an electron dispersive spectrometer (SEM-EDS) was used to provide further insights on the mineralogy and microstructure of the graphite ore specimen, using a FEI 650F scanning electron microscope equipped with two Bruker XFlash 5030 detectors (Institute of Mineralogy and Economic Geology, RWTH Aachen University, Aachen, Germany) (15 kV, 10 nA).

### *2.2. Computed Tomography*

In this study, a ProCon Alpha micro-CT system was used, which is equipped with a five-axes-manipulation system between an XWT-240-TCHE plus X-ray tube with a maximum voltage of 240 kV and an XRD 1611 AP3 detector system with 4064 × 4064 pixels (100 $mm^2$) (Institute of Mineral Resources Engineering, RWTH Aachen University, Aachen, Germany). For the scanning procedure, a cylindrically shaped, polished graphite sample (14 mm diameter, 11.5 mm thickness) was investigated. CT measures the attenuation of an X-ray that passes through sample object [18]. The X-ray attenuation depends on the material density and atomic number as well as the X-ray energy applied [29,30]. A CT measurement is the collection of 2D sample projections (radiographs), which are taken as the sample rotates 360° around the vertical axis between the X-ray tube and the detector. The detector collects the number and intensity of transmitted X-rays of each projection and thus provides X-ray attenuation information. Based on this information, an X-ray attenuation coefficient is calculated for each pixel of the acquired sample projection. This coefficient is displayed as a distinct grey-scale value in the projection image [31]. The collection of radiographs is then stacked to create a 3D volume, comprising a cubical matrix of grey-scale voxels (3D pixels). Thus, CT allows for the 3D analysis of multicomponent materials such as ore and rocks, providing nondestructive internal microstructural information on mineral volume, mineral size, mineral distribution, association, orientation and porosity, e.g., [32–35].

#### 2.2.1. Image Acquisition

Scan parameters were determined in the course of several test measurements and iteratively optimised to obtain low-noise, high-contrast images with as few artefacts as

possible in the shortest possible time. Attenuation curves were calculated based on the samples' mineralogy, as determined by XRD, OM and SEM-EDS (Figure 1).

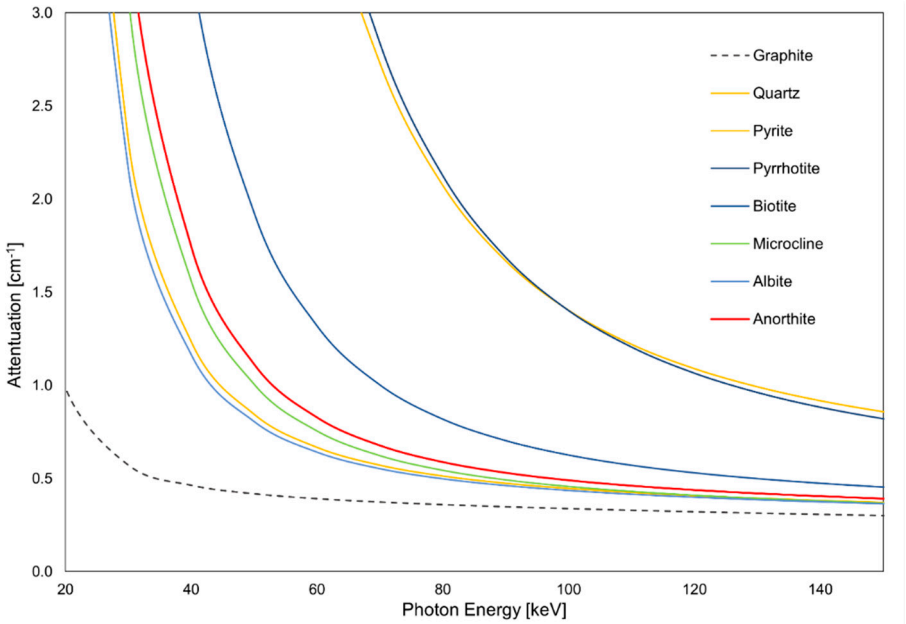



**Figure 1.** Linear attenuation coefficients as a function of X-ray energy for the major minerals occurring in the scanned sample. The values displayed in the graph calculated based on end member compositions, and densities and were calculated using the XCOM Photon Cross-Sections Database NIST [36].

Attenuation curves were calculated by multiplying the mass coefficient by mass density. The nature of X-ray attenuation is predominantly a function of photoelectric absorption and Compton scattering. Photoelectric absorption occurs when the total energy of an incoming X-ray photon is transferred to an inner electron, causing the electron to be ejected. The probability of this effect is heavily dependent on the atomic number (Z) of the absorbing material and the X-ray energy; photoelectric absorption is proportional to $Z^{4-5}$ [36,37]. In Compton scattering, the probability of X-ray absorption is proportional to only Z, as the incoming X-ray photon interacts with a free or outer electron, ejecting the electron. Hence, the probability of this effect is more dependent on the electron density of the material [38]. The photoelectric effect prevails in low energies (approximately 50–100 keV), whereas Compton scattering dominates in energies >5 MeV [39]. Thus, to increase the attenuation contrast between graphite and similar attenuating gangue phases as well as the epoxy resin, the application of lower voltages is recommended. However, using lower voltages results in decreasing penetration capability and the production of more artefacts, especially when high absorbing phases are present. To achieve a good signal-to-noise ratio, a longer exposure time is required in this case, as this is proportional to the number of photons recorded per projection. Thus, given that the sample contains highly absorbing phases, voltage and exposure time were adjusted accordingly to achieve minimum beam hardening on one hand and maximum contrast on the other. To further reduce noise, the number of averages per projection was adjusted accordingly. Lastly, to maintain optimal focal spot size, which determines the X-ray flux and resolution capability of the XCT system, the applied power of the X-ray beam was set slightly higher than the scan resolution. The final scanning conditions are summarised in Table 2.

Reconstruction of the scanned sample was performed with the VGStudio Max 3.5. software [40] based on filtered back-projection (FBP) and a beam hardening correction to address cupping artefacts and streak artefacts generated due to the polychromatic nature of the beam.

**Table 2.** Scanning conditions of the scanned flake graphite ore sample.

| Acquisition Parameters | |
|---|---|
| Voltage [keV] | 100 |
| Current [µA] | 110 |
| Exposure time [s] | 1.35 |
| No. of averages | 4 |
| Binning | 1 × 1 |
| No. of projections | 2500 |
| Scanning time [h:mm] | 9:05 |

#### 2.2.2. Pre-Processing

When the attenuation coefficient values are converted into CT numbers, a certain amount of noise is always present in the CT images due to statistical variations. Therefore, digital image filters were applied prior to segmentation to enhance the quality of the scan by reducing noise and increasing grey value contrast, for example. The actual operation is applied on a 2D CT slice image. The software used, ORS Dragonfly (Version 2022.1) [41], offers a broad range of filtering operations, which can be applied iteratively. A three-filter combination produced the best results (Figure 2). First, a median filter was applied to denoise the image. This was followed by the unsharp filter, using an unsharp factor of 3 to increase the edge contrast of grains. Since the unsharp filter produces noise, the median filter was applied again to denoise the image.

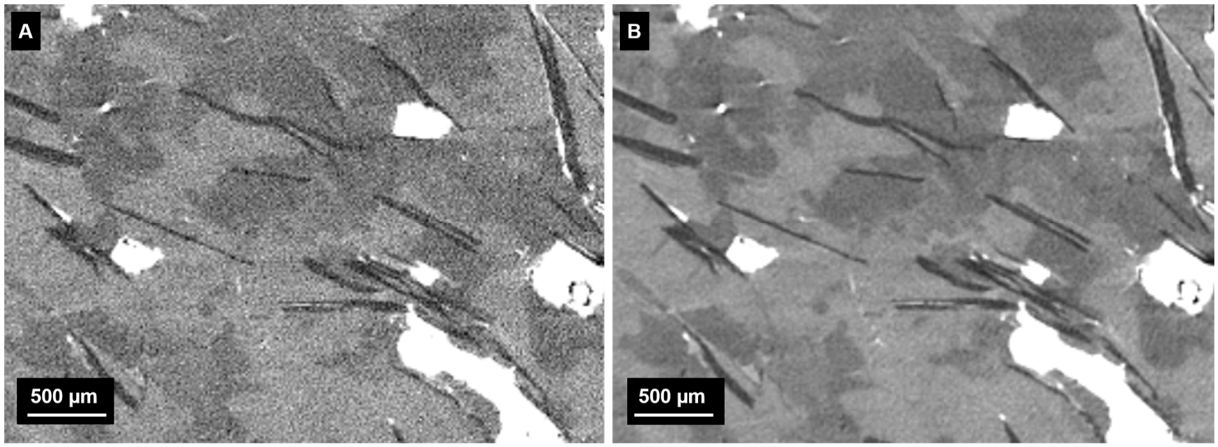



**Figure 2.** CT volume slice before (**A**) and after image filtering (**B**).

#### 2.2.3. Image Processing

Image processing was carried out using ORS Dragonfly. The software possesses different machine learning and deep learning algorithms that can be used for segmenting different phases simultaneously. Machine learning (ML) refers to a class of model-based computational techniques for processing data [42]. Deep learning (DL) is a subset of ML, featuring many interconnected processors (neurons) that work in parallel. These processors are predominately built on a convolutional neural network (CNN) architecture, which is particularly efficient for image processing [43]. To achieve accurate segmentation, the network must be trained to identify structures and learn how to make predictions (inference stage) for subsequent calculations [43]. Therefore, single or multiple regions of interest on different 2D image slices are created and used to manually select groups of voxels which belong to different segmentation classes. These slices are considered ground truth data, on which basis the algorithm is trained and validated (supervised classification). Consequently, the network allows for automatic segmentation of the entire data set.

The segmentation procedure was performed on a digitally cut cylindrical subvolume (10.53 mm diameter, 8.21 mm thickness) so that (a) the epoxy mount, in which the section

was embedded, was excluded as well as the cone-beam effect (depth-related greyscale gradients); (b) operation time was accelerated by reducing the data size; (c) each horizontal slice was of equal area; and (d) the topmost slice had the same surface as that of the polished section to enable subsequent comparison with mineralogical and petrographic OM and SEM-EDS data. Regarding the model architecture, Random Forest [44], U-Net [45] and sensor3D [46] models were tested and trained. The mineralogical and petrographic information obtained using XRD, SEM-EDS and OM was essential to interpret the CT radiographs and to identify the phases according to their grey-scale values. Three classes were determined, comprising graphite, high X-ray attenuating phases (i.e., pyrite, pyrrhotite, rutile, zircon) and the remaining gangue minerals. These were labelled manually on a randomly selected area (frame) of a 2D slice to establish a first training data set. The model was then tested on a new slice, and wrongly classified voxels were corrected and attributed to the training data. The accuracy of a model and thus the segmentation result depends on the network parameters, which need to be selected properly in accordance with the properties of the data information to be segmented. After several trial runs with different combinations of parameters and training slices, the sensor3D network was identified to perform best, and therefore, it was used for subsequent segmentation operations until no further improvement could be achieved (Figure 3).

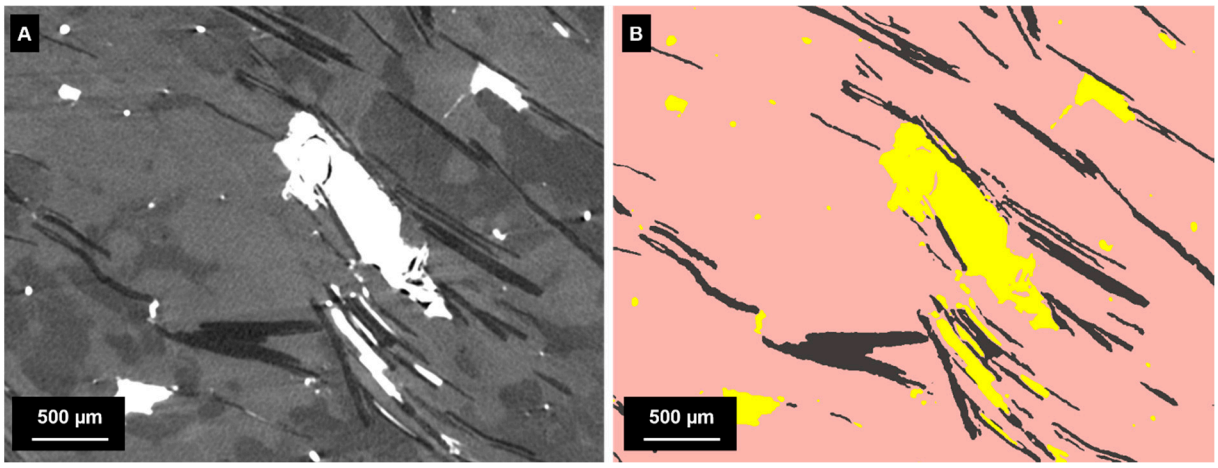



**Figure 3.** CT volume slice of the scanned specimen before (**A**) and after segmentation (**B**). The colours represent the segmented classes: graphite (dark grey), high X-ray absorbing phases (particularly pyrrhotite, pyrite and accessories of zircon) (yellow) and the silicate matrix (pink).

The final model architecture is summarised in Table 3. In total, 6 frames were created, and the training time was 216 min. A total of 80% of the labelled data were selected by default for training the model and the remaining 20% for validating the model. Furthermore, the sensor3D model was trained for 20 epochs with early stopping enabled to avoid overfitting, whereby the model stopped automatically if the validation loss increased. The model applied reached a dice coefficient of 0.9971, which is an indicator of the model's accuracy.

**Table 3.** Model architecture of the DL network.

| Model Parameter | Value | Explanation |
|---|---|---|
| Patch size | 64 | Size of the areas (patches) into which the input image is divided |
| Batch size | 32 | Input layer, defines number of patches being evaluated |
| Epochs per frame | 20 | One training operation |
| Stride-to-input ratio | 0.1 | Defines the position of the neighbouring patches |
| Dice score | 0.9971 | Measurement of the precision of a deep learning model based on the similarity of prediction and ground truth data |

## 3. Results

### *3.1. Mineralogy and 2D Petrography*

The flake graphite ore samples consist of a quartz-dominated matrix with plagioclase (anorthite and albite), microcline, biotite, pyrite and pyrrhotite as well as small quantities of rutile, clinochlore and clay minerals. Zircon is present as an accessory. Foliation structure is present primarily due to graphite and biotite ± clinochlore arrangement. Graphite occurs as deformed euhedral–subhedral, platy-shaped crystals, varying in grain size from ~15 to 1900 µm, with most of the flakes >100 µm. The graphite particles are mostly disseminated in the matrix with some large particles attached to each other. Some flakes are deformed and broken apart along the cleavage plains. The grain boundaries of the flakes are of straight or polygonal structure. Quantities of rutile as well as pyrrhotite and pyrite are present as subhedral to euhedral crystals in the matrix. Both pyrite and pyrrhotite are occasionally attached to graphite flakes, where they may occur as elongated crystals along basal cleavage planes of graphite (Figure 4). Biotite is occasionally moderately replaced by clinochlore and mostly associated with graphite. Clay minerals are present along cracks, cleavages of feldspar and grain boundaries. Given the high quartz content, secondary minerals and foliation texture, the ore can be considered an altered graphite gneiss.

### *3.2. Computed Tomography*

Figure 5 shows a CT volume slice from the scanned flake graphite ore sample. The assignment of grey values to their corresponding phases was based on the XRD, SEM-EDS and OM examinations. Graphite appears dark grey and can be recognised by its typical flaky shape. The phases with the brightest grey values are pyrites and pyrrhotites. In addition, two grey value ranges can be identified: (1) combined quartz, plagioclase and clay minerals, as well as (2) combined biotite, clinochlore and microcline feldspar. The differentiation between the individual minerals within the respective grey value ranges is not possible, as their grey values are too similar.

For the quantitative analysis of the CT data, the volume, aspect ratio and voxel count were calculated from the segmented classes. Based on these parameters, the graphite volume was refined so that particles wrongly labelled as graphite could be removed from the segmented data. To ensure that realistic grain shapes could be imaged, only particles <4.64 × 4.64 × 4.64 µm (100 voxels) were considered for the analysis. A total of 1877 graphite particles were identified. The segmented volume comprises 533.99 $mm^3$ and the graphite volume 19.77 $mm^3$. This corresponds to a volumetric proportion of 3.7% graphite (Table 4).

Figure 6 shows the individual graphite particles (Figure 6A), comprising the sample as well as their volumetric distribution (Figure 6B) in 3D. Graphite flakes are aligned and occur mostly disseminated in the ore matrix. The flakes exhibit a subhedral to euhedral shape and vary in grain size. A few, and particularly larger, flakes are subparallel to parallel attached together.

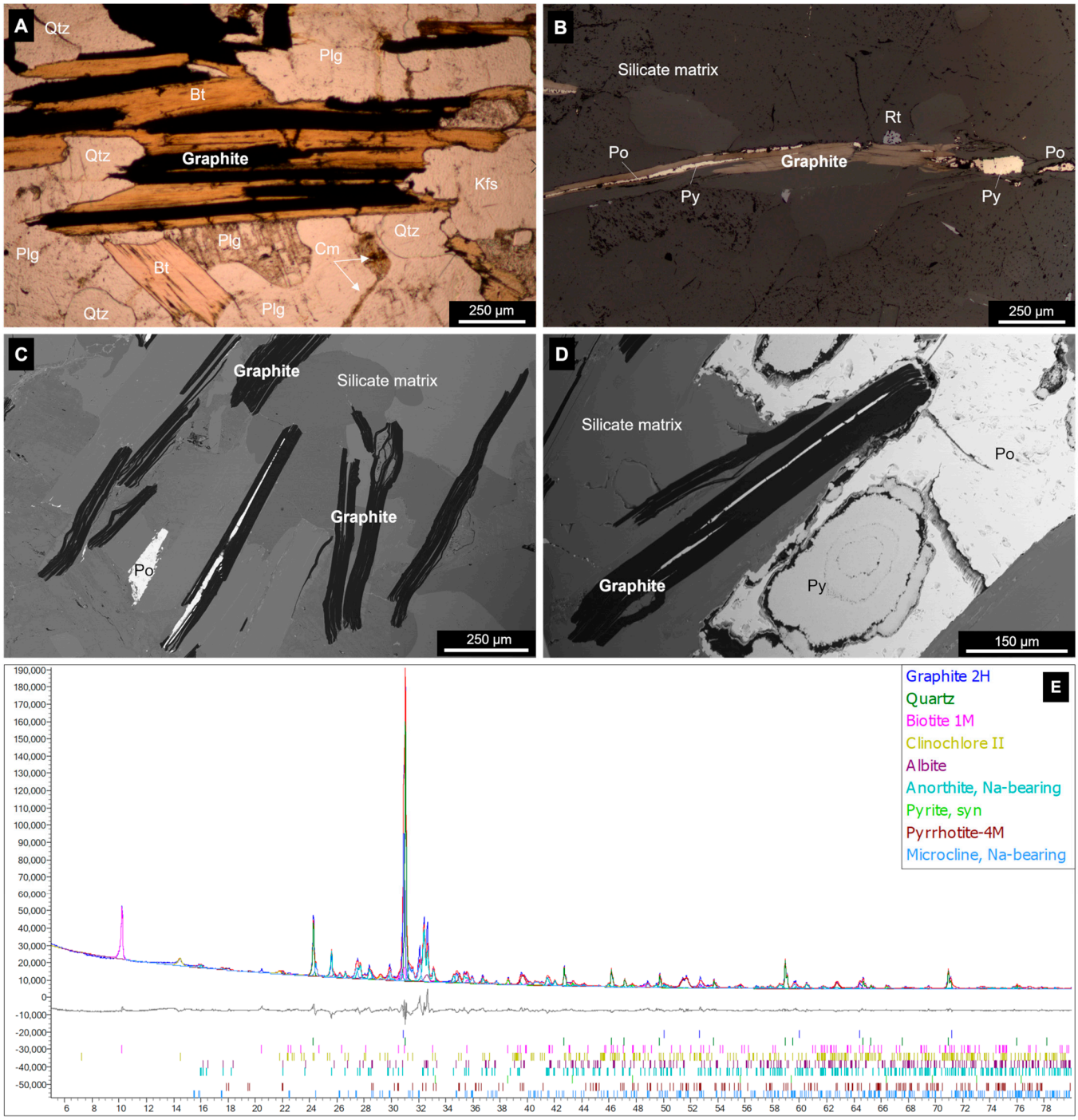



**Figure 4.** OM (**A**,**B**), SEM images (**C**,**D**) and (**E**) XRD patterns of the flake graphite ore sample. (**A**) Parallel aligned graphite flakes intergrown with biotite. Graphite flakes are embedded in a silicate matrix comprising quartz, plagioclase (anorthite and albite), biotite and alkali feldspar (microcline). Secondary clay minerals occasionally replace plagioclase and appear along grain boundaries (transmitted light, PPL). (**B**) Disseminated super jumbo flake with intergrowth of pyrite and pyrrhotite along basal cleavage planes embedded in silicate matrix. Pyrite, pyrrhotite and rutile are also present as subhedral crystals (reflected light, PPL). (**C**) Disseminated parallel to subparallel oriented graphite flakes, partly deformed and broken apart along basal cleavage planes. (**D**) Graphite flake intergrown with a subhedral crystal of pyrrhotite. Note the colloform nodule of pyrite in the pyrrhotite grain. Abbreviations: Po = pyrrhotite, Py = pyrite, Qtz = quartz, Bt = biotite, Kfs = alkali feldspar, Plg = plagioclase, Rt = rutile, Cm = clay minerals, PPL = plane-polarised light.

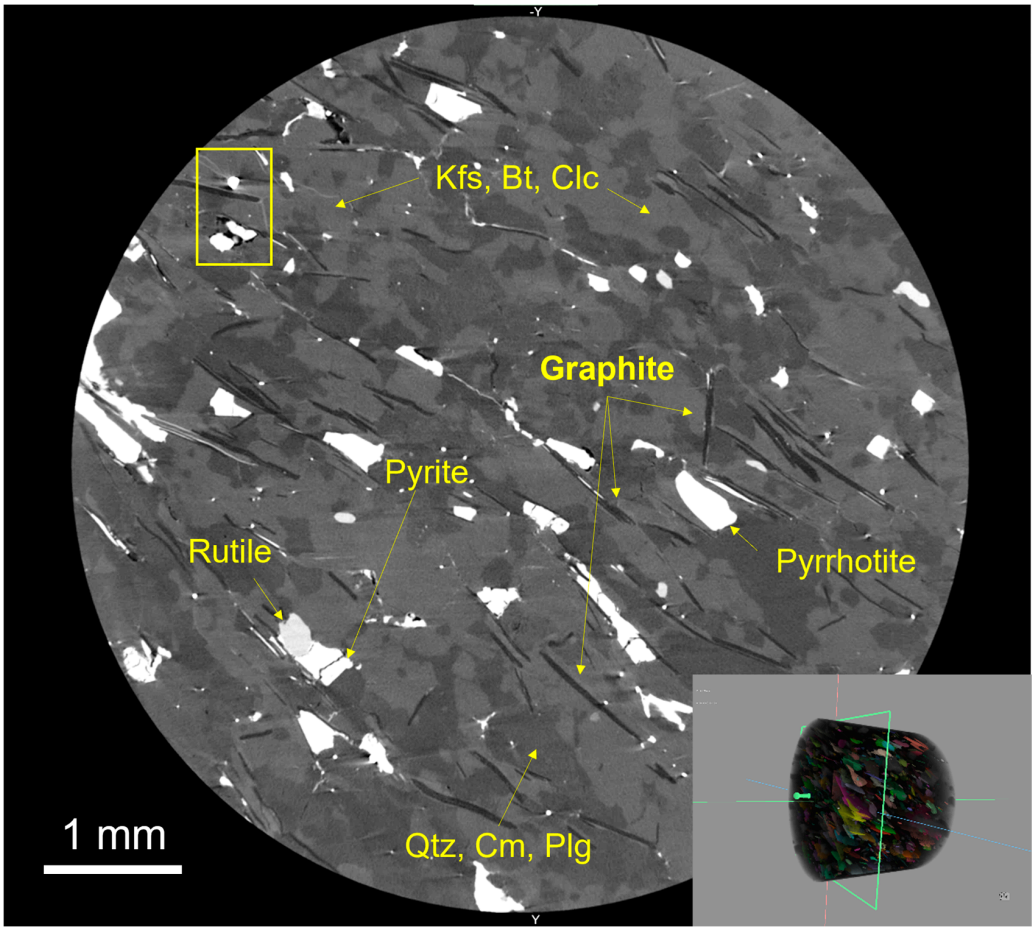



**Figure 5.** CT volume slice of the cylindrical subvolume of the scanned graphite sample. Note the imaging artefacts in the yellow framed box (bright shining streaks above a graphite flake and dark areas between and around two Po crystals) due to the highly X-ray absorbing iron phases present in the sample. Abbreviations: Qtz = quartz, Bt = biotite, Kfs = alkali feldspar, Plg = plagioclase, Clc = clinochlore, Cm = clay minerals.

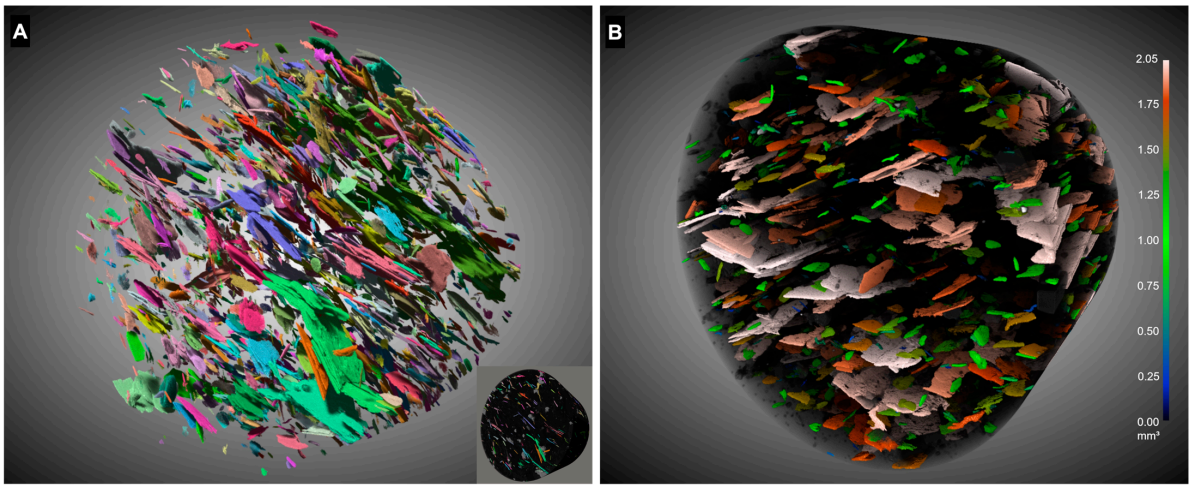



**Figure 6.** Three-dimensional CT images of the cylindrical subvolume after segmentation: (**A**) colour-coded graphite particles and (**B**) volumetric distribution of the graphite flakes. The gangue minerals comprising the ore matrix are semitransparent. The cylinder has a diameter of 10.53 mm and a thickness of 8.21 mm.

**Table 4.** Segmentation and analysis results of the sample.

| Properties of the Subvolume | |
|---|---|
| Length | 8 mm |
| Diameter | 10.53 mm |
| Volume cylinder | 533.99 $mm^3$ |
| Volume graphite | 19.77 $mm^3$ |
| Volume % graphite | 3.7% |
| Number of graphite particles | 1877 |

To assess the quality of the sample based on the grain size distribution, the equivalent spherical diameter was calculated using the volume of each particle (Equation (1)).

$$ESD = \sqrt[3]{\frac{6 \times volume}{\pi}} \quad (1)$$

Figure 7A shows the cumulative in situ particle size distribution of graphite as determined by CT. In terms of particle numbers, small flakes represent the largest proportion of all particles, followed by amorphous and large flake particles (Figure 7B). In relation to the volume of all graphite particles, super jumbo flakes account for the highest proportion of all classes (Figure 7C). Properties of each class are summarised in Table 5.

The volumetric distribution of the classes is also illustrated in Figure 8. By highlighting the individual graphite classes (Figure 8B–E), it becomes apparent that especially the super jumbo and jumbo fractions are occasionally parallel to subparallel attached to each other. The other classes are predominantly disseminated throughout the matrix.

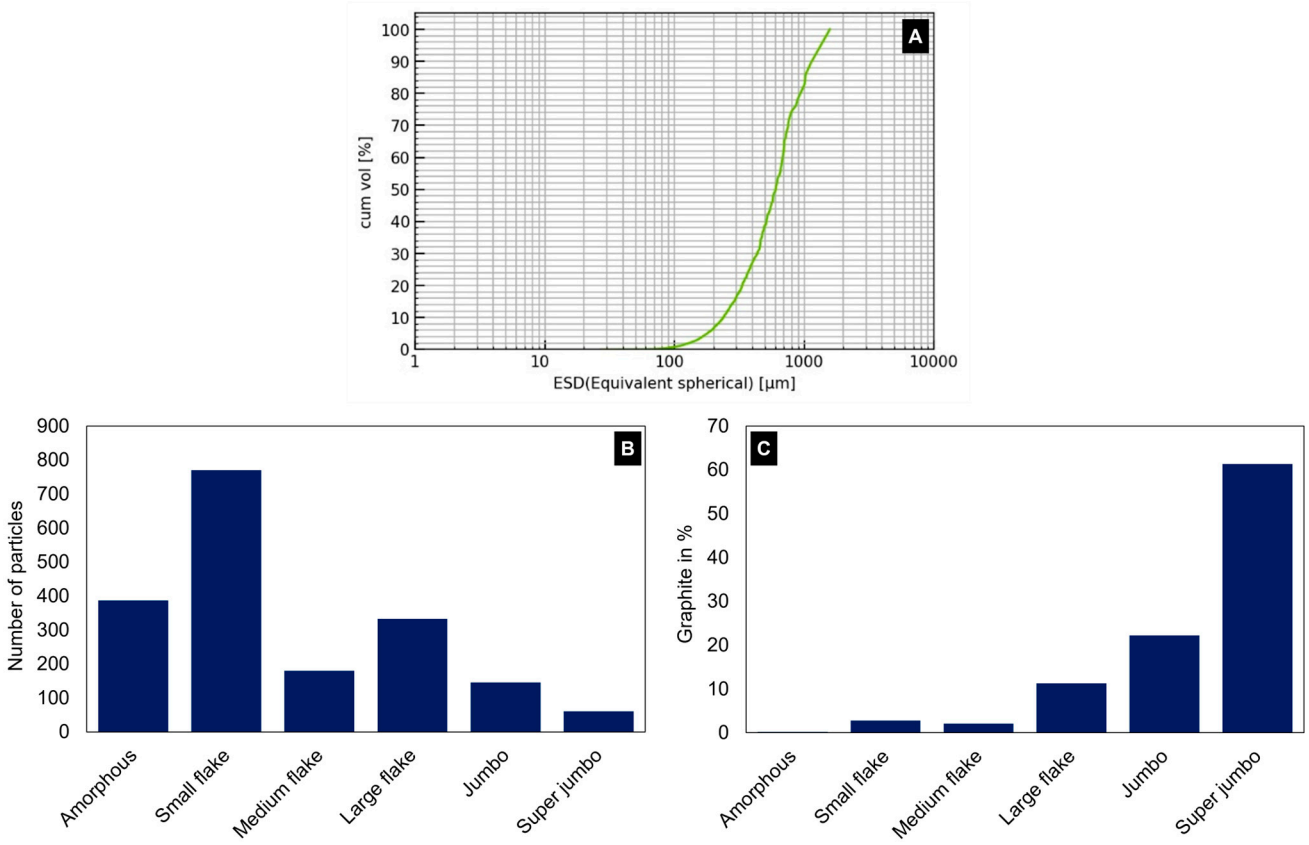



**Figure 7.** Distribution of graphite types according to CT measurements. (**A**) Cumulative particle analysis, (**B**) number of particles corresponding to each class and (**C**) volumetric proportion of each class in the sample.

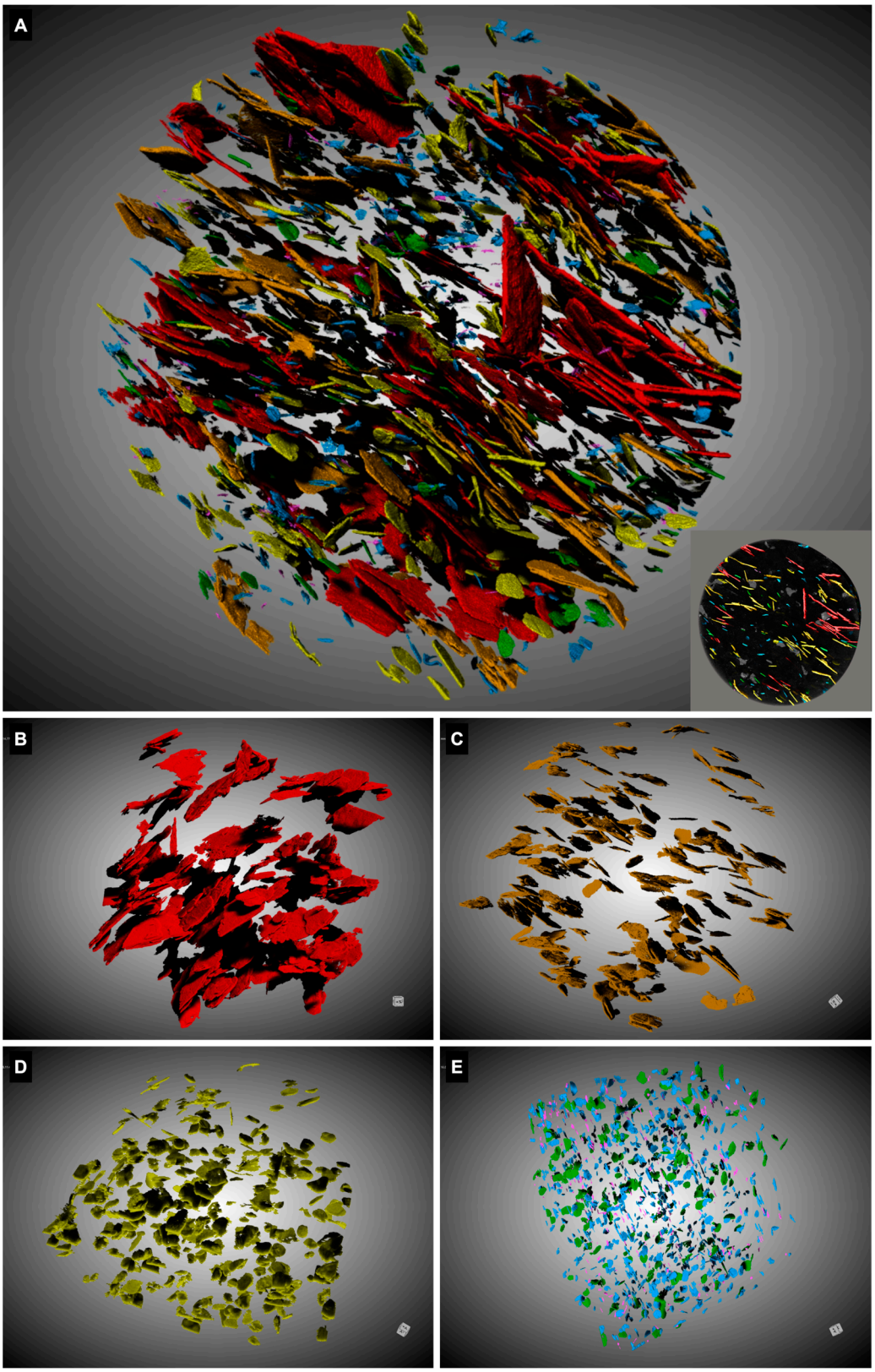



**Figure 8.** Three-dimensional CT images of the segmented subvolume. (**A**) Volumetric distribution of the graphite flakes in terms of market-related classes comprising super jumbo size (red), jumbo (orange), large flake (yellow), medium flake (green), small flake (blue) and amorphous (violet). The gangue matrix is set fully transparent. A corresponding video is provided in Supplementary Materials. Figure 8B–E individual classes highlighted: (**B**) super jumbo size flakes, (**C**) jumbo flake graphite, (**D**) large flake graphite and (**E**) combined medium flake (green), small flake (blue) and amorphous graphite (violet).

**Table 5.** Properties of the graphite classes determined.

| | Amorphous | Small Flake | Medium Flake | Large Flake | Jumbo | Super Jumbo |
|---|---|---|---|---|---|---|
| Particles (n) | 387 | 770 | 180 | 333 | 146 | 61 |
| Particles (%) | 20.62 | 41.02 | 9.59 | 17.74 | 7.78 | 3.25 |
| Volume ($mm^2$) | 0.05 | 0.55 | 0.42 | 2.23 | 4.4 | 12.13 |
| Volume (%) | 0.23 | 2.78 | 2.11 | 11.28 | 22.23 | 61.36 |

Since graphite deposits can be very heterogeneous in terms of flake size and graphite content distribution, it is important to measure a large and representative sample volume. Figure 9 illustrates the distribution of graphite concentration from top to bottom in the cylindrical subvolume. For this purpose, the graphite concentration for each slice was measured by subtracting the segmented graphite area per slice from the area of the cylinder. In total, 1550 slices were measured, with a thickness of 0.0053 mm per slice. The graphite concentration varies significantly throughout the volume, from 2.46 to 6.97%. Particularly in the upper range of the subsample (slice 0 to 60), the graphite concentration is higher than in the rest of the sample, where the concentration varies from 2.46 to 4.66%.

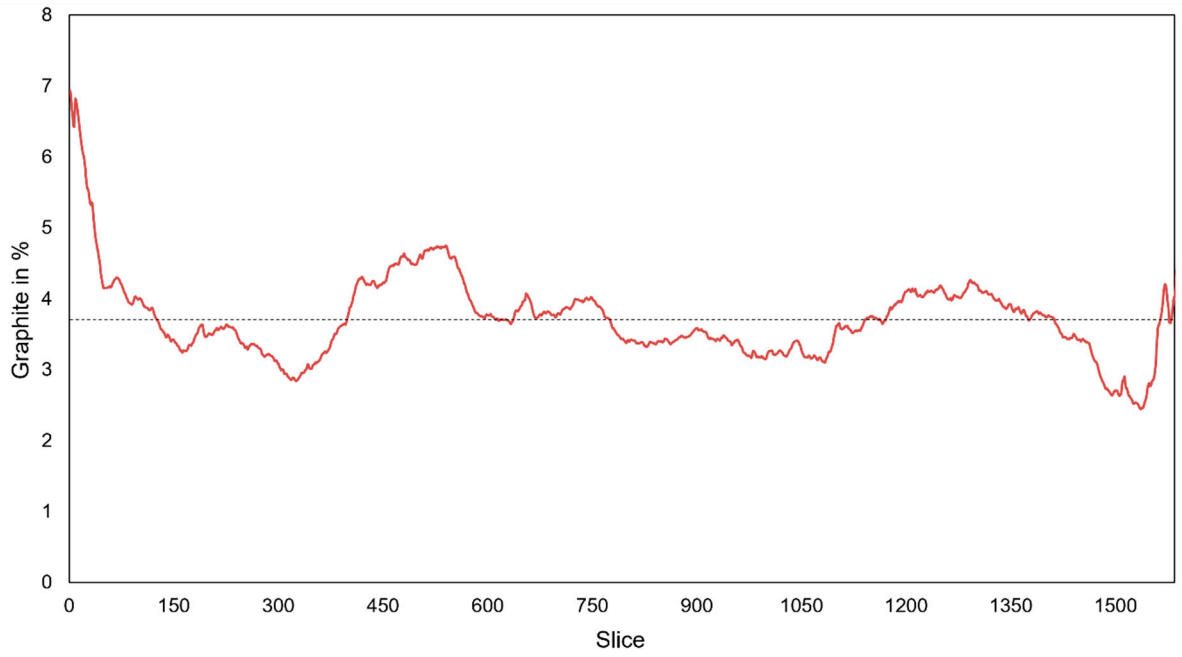



**Figure 9.** Graphite content per slice of the cylindrical subvolume. The dashed horizontal line represents the average graphite concentration of 3.7%.

In addition to particle size distribution and graphite content, textural properties such as flake thickness or impurities also play an important role in the evaluation of a graphite ore. Figure 10 shows the analytical result of a single particle, exemplified by grain thickness. A jumbo flake with an ESD of 421 µm and a volume of 0.04 $mm^3$ was extracted from the segmented graphite volume, and for the thickness measurement, the particle volume was extracted to a surface mesh. The differences in the colour markings indicate the differences in thickness along the flake. The average thickness is 56 µm. Further textural properties are listed in Table 6.

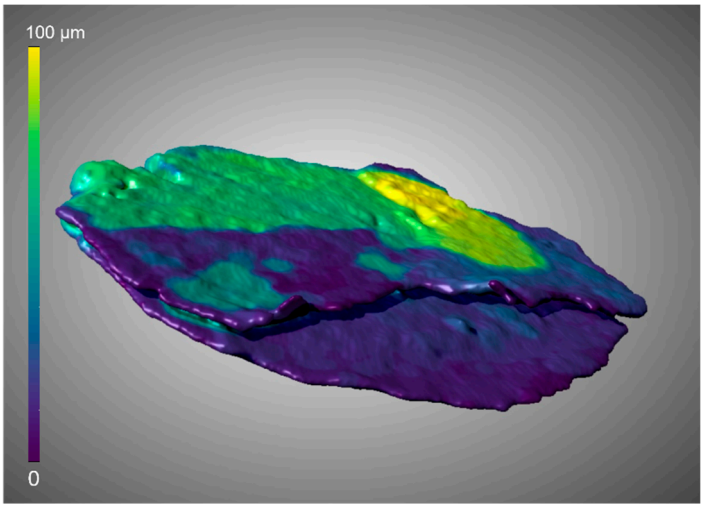



**Figure 10.** Jumbo flake after thickness measurement. The ESD of the flake is 421 µm.

**Table 6.** Selected textural properties of an individual graphite flake.

| Flake Properties | |
|---|---|
| Volume | 0.04 $mm^3$ |
| ESD | 421 µm |
| Thickness (mean) | 56 µm |
| Feret diameter (max) | 1196 µm |
| Feret diameter (min) | 497 µm |
| Surface area | 2.3 $mm^2$ |

Figure 11 features a subhedral graphite flake associated with an iron sulfide grain. In contrast to the 2D image, the 3D image exhibits that the flake is not only attached to the iron sulfide but also intergrown with it.

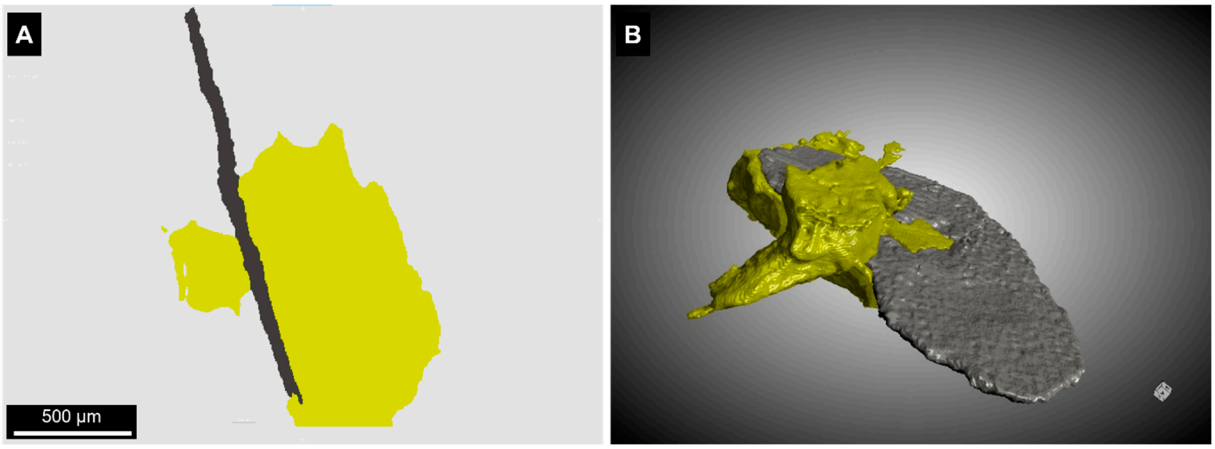



**Figure 11.** Jumbo-sized flake associated with an iron sulfide mineral in 2D (**A**) and 3D (**B**). The CT volume slice (**A**) shows that the graphite flake is attached to the sulfide mineral. By contrast, the rendered 3D image (**B**) reveals that the sulfide mineral is intergrown with the graphite flake. The longest axis of the flake is 1690 µm.

### *3.3. Comparison of 2D Petrographic Data with 3D CT Data*

To evaluate the validity of the CT results, a modal mineralogy analysis obtained from optical microscopy analyses was compared with the topmost slice of the CT sample volume (Figure 12). This slice was not part of the segmented cylinder due to abundant

imaging artefacts. The topmost slice was trained using the same DL strategies as described above. A set of microphotographs was stitched together to reveal the total surface of the polished section. The stitched image was processed using ORS Dragonfly, applying a global threshold operation. Thereby, the graphite content was measured by subtracting the area of segmented flakes from the total area (86.92 $mm^2$). According to the OM analysis, the graphite content is 3.3%. The graphite content of the topmost CT volume slice is 2.99%, which is a difference of 9.39% compared to the OM measurement.

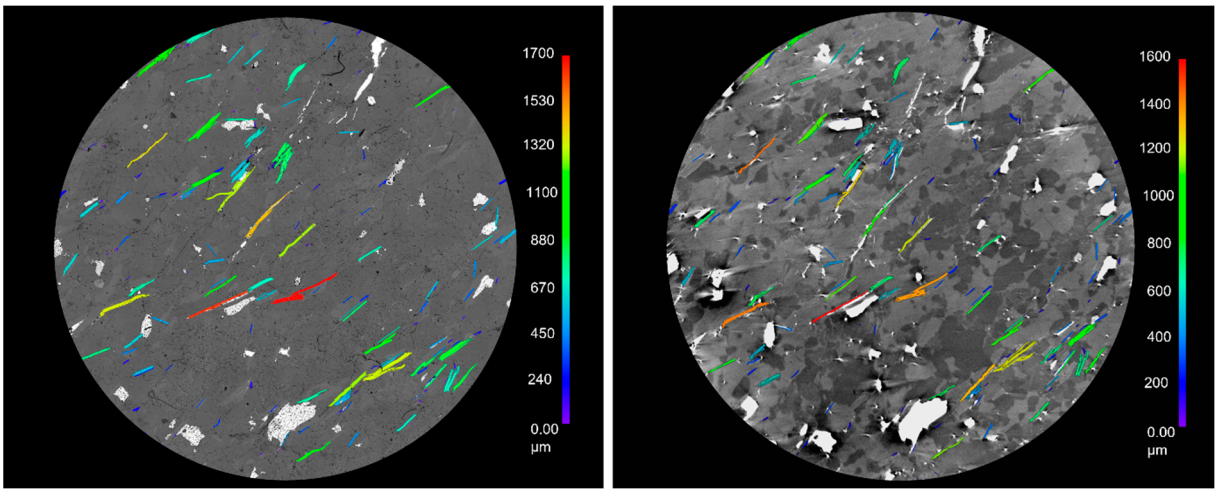



**Figure 12.** Segmentation result of the CT volume topmost slice and the stitched OM image. The rainbow-coloured scale shows the distribution of the longest axis of the individual flakes.

Details of graphite analyses as performed by OM and CT are given in Tables 7 and 8. A total amount of 169 graphite flakes were identified using OM (Table 7), whereas 156 flakes were identified in the topmost slice using CT imaging (Table 8). In particular, more amorphous and small flake grains were found with OM compared to CT. On the other hand, more jumbo flakes were identified in the topmost slice by CT. Overall, the relative proportion of graphite in each class is similar for both OM and CT, with the exception of the jumbo and amorphous classes (Figure 13).

**Table 7.** Physical properties of graphite as determined by OM in a polished section.

| | Amorphous | Small Flake | Medium Flake | Large Flake | Jumbo | Super Jumbo | Total |
|---|---|---|---|---|---|---|---|
| Particles (n) | 26 | 20 | 11 | 31 | 25 | 56 | 169 |
| Particles (%) | 15.38 | 11.83 | 6.51 | 18.34 | 14.79 | 33.14 | 100 |
| Area ($mm^2$) | 0.02 | 0.04 | 0.04 | 0.09 | 0.24 | 2.44 | 2.87 |
| Area (%) | 0.63 | 1.44 | 1.27 | 3.07 | 8.50 | 85.09 | 100 |

**Table 8.** Physical properties of graphite as determined by CT in the topmost slice after segmentation.

| | Amorphous | Small Flake | Medium Flake | Large Flake | Jumbo | Super Jumbo | Total |
|---|---|---|---|---|---|---|---|
| Particles (n) | 22 | 20 | 10 | 20 | 35 | 49 | 156 |
| Particles (%) | 14.10 | 12.82 | 6.41 | 12.82 | 22.44 | 31.41 | 100 |
| Area ($mm^2$) | 0.02 | 0.06 | 0.05 | 0.15 | 0.44 | 1.87 | 2.60 |
| Area (%) | 0.77 | 2.43 | 1.78 | 5.96 | 16.90 | 72.16 | 100 |

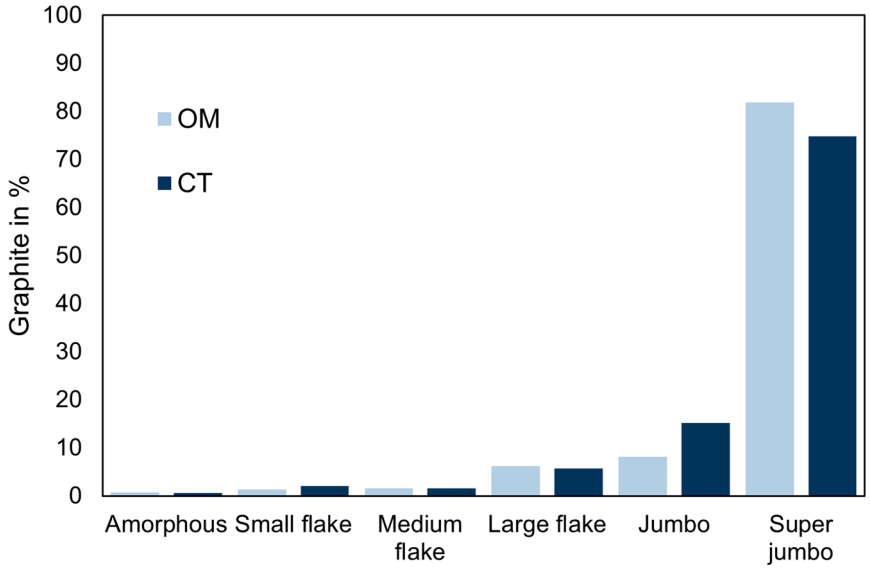



**Figure 13.** Histogram showing the size distribution of graphite, as determined on a polished section using OM and on the sample volume topmost slice using CT.

## 4. Discussion

### *4.1. Graphite Characterisation*

In recent years, an increasing number of scientific studies have recognised the utility of CT for ore characterisation [19–27]. Despite this, the application of CT to characterise graphite raw materials is limited, with prior studies having only provided rudimentary descriptions of graphite through the use of CT. Ren et al. examined drill cores of graphite ore using CT to distinguish minerals with high and low X-ray attenuation [47], while Fatima et al. analysed the spatial distribution of various ore minerals, including graphite, with CT [48].

Traditionally, information on graphite ore mineral properties is obtained by XRD, sieve analysis, SEM-EDS or OM examination, e.g., [16,49,50]. These methods provide liberation sizes with accuracies of <120–150 µm [51]. SEM-based automated mineralogy has been recently introduced to establish more precise liberation information [16]. Furthermore, the method provides quantitative information on impurities, grain size distribution and modal mineralogy. MLA thereby extracts information on modal mineralogy on 2D surfaces and mineral associations, which are based on linear contacts and phases exposed at the samples' section surface. For ores with a heterogeneous grain size distribution, this may lead to erroneous information (Figure 9). Moreover, graphite is a very soft mineral and may be affected by mechanical abrasion during sample preparation [16]. This can result in misinterpretations of key textural features. CT, in contrast, as demonstrated in this study, can assess a more representative volume and modal mineralogy nondestructively without stereological bias.

Information on graphite impurities is vital. During graphite ore genesis, other minerals may be deposited between graphite layers, stacks or clusters. Such impurities are attached to flake surfaces or are trapped between flakes (intercalated) [52]. Impurities adhering to the surface can be detached from the flake surface by attrition, without significantly influencing flake size. Those impurities between the layers can only be removed by additional thermal or chemical processes, and such ore treatment methods are cost-intensive. Characterising impurities appropriately is therefore crucial to effectively remove this material. Such information on impurities (Figure 11), as provided by 3D CT imaging, allows the appropriate design of flow sheets for the beneficiation of graphite ores.

The results demonstrate that CT is an excellent addition to conventional methods such as XRD, OM and SEM to extract key microstructural information for assessing the quality of a graphite ore. While established techniques exhibit better resolutions and infor-

mation on the gangue mineralogy, they do not present information about the real spatial distribution and volume fraction of graphite within ore samples. CT provides exceptional 3D microstructural data of graphite ore and a more representative characterisation of the quality demanding properties of graphite particles such as in situ grain size, grain size distribution, shape and impurities. In addition, the CT method enables precise measurement of individual flake thickness (as shown in Figure 10 and Table 6), which is important for predicting flake breakage during liberation. Thin flakes are more prone to breaking during comminution, making it more difficult to maximize their size. Knowledge on particle thickness therefore aids in selecting the appropriate comminution technique. Lastly, it is also possible to generate 3D information on individual grains and their impurities (Figure 11).

### *4.2. CT Data Acquisition*

In order to acquire valid CT images and data on geological materials, the mineralogy of the samples needs to be known. Thus, CT cannot be used as a stand-alone technique. Mineralogical methods such as XRD and OM are required to acquire and interpret CT data. Moreover, CT operation requires an experienced operator to achieve appropriate results, particularly for the resolution of minerals with similar attenuation coefficients. The contrast of the grey-scale image in the CT depends on different factors such as X-ray energy applied, as well as the atomic number and density of the phases comprising the sample measured [31]. The choice of the optimal beam intensity to resolve all minerals is infinite. As the investigated ore is rich in heavy minerals such as pyrite and pyrrhotite, it would have required high beam intensities for adequate X-ray penetration to prevent artefacts. This, however, decreases the X-ray absorption capacity of the lower absorbing minerals such as graphite, and silicates, because the attenuation using X-ray energies >100 kV is more sensitive to the mineral's density [38]. Choosing lower X-ray energies would have increased the attenuation differences between lower absorbing fraction (Figure 1) as it is more sensitive to the atomic number [39], but it would have also increased beam hardening, particularly due to the presence of the iron sulfides. A possible solution to achieve high contrasts of the low X-ray attenuating minerals and to minimise beam hardening would be to combine multiple scans with different X-ray intensities. However, as the primary goal was to differentiate graphite from the gangue material, the acquisition parameter selected to image the graphite ore showed a good balance between contrast and beam hardening prior to the high absorbing phases. Thus, it was possible to differentiate between graphite, pyrite, pyrrhotite, rutile and silicate matrix based on the grey-scale contrast of the CT image.

Even though good scan quality was achieved, minerals may exhibit a large range of grey-scale values due to the polychromatic nature of X-rays and the co-occurrence of minerals with different X-ray attenuation. Reliable mineral segmentation of CT data, particularly of complex rock samples such as the specimen used for this study, is therefore challenging. However, using the deep learning algorithms for segmentation as featured by ORS Dragonfly, segmentation of minerals does not solely rely on grey value contrast, as it also considers textural features such as grain shape. By providing the DL model sufficient training data, it was possible to differentiate between areas exhibiting the same grey values. Such areas also contained imaging artefacts, produced by high-absorbing sulfide minerals (Figure 5) as well as gangue material.

The accuracy of the segmentation method, however, may be limited due to certain factors. The first factor is the partial volume effect (PVE) [31]. If a single voxel consists of more than one phase, the CT number represents the average of the X-ray attenuation of all phases present. Consequently, all particles below voxel size are affected by the PVE and cannot be imaged. Directly related to the PVE is the blurring of the CT data, particularly in samples with phases of large attenuation differences, as in the investigated specimen [53]. Blurring complicates the quantitative interpretation of CT data, particularly at grain boundaries and for small particles, as it causes each voxel to contain portions of the surrounding voxels. Consequently, phases approaching the spatial resolution of the CT

data also contain voxels that reflect the surrounding material. Segmentation will therefore lead to an over- or underestimation of the labelled volume [54]. One way to minimise the effect is to increase the image resolution, but this comes at the cost of sample size. Another method is to refine the segmentation result by eroding or dilating the segmented volume. However, it is not possible to fully eliminate these artefacts as they originated from the voxelised data themselves. In addition to imaging artefacts, another source of error is derived from the manual segmentation process that must be conducted to provide the training data and at the inference stage. These are the most exhausting steps, and there will inevitably be some inadvertent errors in labelling among the large number of pixels (4096 × 4096) comprising each slice. Consequently, there will be some judgement errors for pixels located at grain boundaries and those reflecting small particles, due to the above mentioned PVE and blur artefacts but also regardless of them. Therefore, to minimise this bias, only graphite flakes comprising >100 voxels (ca. 25 µm ESD) were considered for the analysis.

A comparison of the topmost CT sample slice with the stacked OM image shows good agreement in terms of graphite content, number of particles and grain size distribution. However, several factors must be considered that hinder a direct comparison. Due to blurring, a complete overlap of the two cut surfaces was not possible. Further, the slight difference in the size of individual flakes (Figure 12) and number of jumbo flakes, large flakes and super jumbo flakes (Tables 6 and 7) may be explained by the fact that some flakes were not yet connected to the 2D radiograph and/or were incorrectly identified as two separate or one entire grain, respectively, because of the PVE. The PVE also affects the calculation of the total graphite content, as it results in an under- or overestimation of the segmented surface, as mentioned above. The lower number of identified amorphous flakes in the CT image can be attributed to both the scanning resolution and the PVE. Lastly, the slice was not part of the segmented volume as it represents the topmost slice of the cylinder. As mentioned above, the topmost slice is more affected by artefacts than inner slices. Surfaces that are parallel to the X-ray beam at the top and bottom of the sample will not penetrate properly, which will lead to image artefacts and thus a lack of detail in the data. Consequently, to be able to include the topmost slice in the volume, the scanning geometry should be mounted at a slight angle to avoid parallel alignment of the circular base and top surfaces of the cylinder to the X-ray beam. This reduces artefacts and thus enables a better comparison.

## 5. Conclusions

This study explored the use of CT for establishing the physical properties of graphite in geological ores. The results reveal that CT is a valid and innovative technique that can be effectively used to characterise graphite. It enables nondestructive, in situ 3D visualisation and provides quantitative information on critical mineralogical aspects such as flake size, flake size distribution, shape and impurities that cannot be determined with other currently available analytical tools.

Given that graphite raw materials should be assessed by their mineralogical properties [9–11,13], the additional information provided by CT should allow improved resource recovery and beneficiation processes. By obtaining in situ information on flake size, flake size distribution and flake thickness before and after comminution, the yield of the process may be quantified. Thus, CT can provide information on ore characteristics and impurities in 3D, which may help to further improve the process design.

Prior knowledge on the samples' mineralogy is required to appropriately acquire quantitative CT data and allow the possibility of differentiating between similar attenuating phases. Furthermore, the resolution of CT is not as high as, for example, OM or SEM-EDS. Against this background, CT cannot be used as a stand-alone technology. Hence, in combination with traditional methods, CT analyses allow for an improved understanding of graphite ores and products.

**Supplementary Materials:** The following supporting information can be downloaded at: https://www.mdpi.com/article/10.3390/min13020247/s1, Video S1: Graphite classes.

**Author Contributions:** Conceptualisation, L.T.K.; methodology, L.T.K.; formal analysis, L.T.K.; investigation, L.T.K. and X.L.; data curation, L.T.K.; writing—original draft preparation, L.T.K.; writing—review and editing, L.T.K. and B.G.L.; visualisation, L.T.K.; project administration, L.T.K. All authors have read and agreed to the published version of the manuscript.

**Funding:** This research was funded by the Exploratory Research Space of the RWTH Aachen University, grant number SFUoA001.

**Data Availability Statement:** Data supporting the findings of this study will be made available from the corresponding author, upon reasonable request.

**Acknowledgments:** The authors thank NGS Trading & Consulting GmbH for providing the sample used in this study. The authors are also grateful to four anonymous reviewers for their helpful and constructive feedback.

**Conflicts of Interest:** The authors declare no conflict of interest.

## References

1. Chung, D.D.L. Review Graphite. *J. Mater. Sci.* **2002**, *37*, 1475–1489. [CrossRef]
2. Pierson, H.O. *Handbook of Carbon, Graphite, Diamonds and Fullerenes: Processing, Properties and Applications*; William Andrew: Norwich, NY, USA, 2012; ISBN 9780815517399.
3. Bessel, C.A.; Laubernds, K.; Rodriguez, N.M.; Baker, T.K. Graphite Nanofibers as an Electrode for Fuel Cell Applications. *J. Phys. Chem. B* **2001**, *105*, 1115–1118. [CrossRef]
4. European Commission. *Study on the EU's list of Critical Raw Materials*; European Commission: Luxembourg, 2020.
5. U.S. Geological Survey. List of Critical Minerals. Available online: https://www.usgs.gov/news/national-news-release/us-geological-survey-releases-2022-list-critical-minerals (accessed on 19 December 2022).
6. U.S. Geological Survey. *Mineral Commodity Summaries—Graphite*; USGS: Reston, VA, USA, 2022.
7. Simandl, G.J.; Paradis, S. Graphite deposit types, their origin, and economic significance. *Br. Columbia Minist. Energy Mines Br. Colomb. Geol. Surv.* **2015**, *3*, 163–171.
8. Luque, F.J.; Huizenga, J.-M.; Crespo-Feo, E.; Wada, H.; Ortega, L.; Barrenechea, J.F. Vein graphite deposits: Geological settings, origin, and economic significance. *Min. Depos.* **2014**, *49*, 261–277. [CrossRef]
9. Chehreh Chelgani, S.; Rudolph, M.; Kratzsch, R.; Sandmann, D.; Gutzmer, J. A Review of Graphite Beneficiation Techniques. *Miner. Process. Extr. Metall. Rev.* **2016**, *37*, 58–68. [CrossRef]
10. Jara, A.D.; Betemariam, A.; Woldetinsae, G.; Kim, J.Y. Purification, application and current market trend of natural graphite: A review. *Int. J. Min. Sci. Technol.* **2019**, *29*, 671–689. [CrossRef]
11. Damm, S. *Rohstoffrisikobewertung—Graphit*; Deutsche Rohstoffagentur (DERA) in der Bundesanstalt für Geowissenschaften und Rohstoffe (BGR): Berlin, Germany, 2021; ISBN 3948532486.
12. Moradi, B.; Botte, G.G. Recycling of graphite anodes for the next generation of lithium ion batteries. *J. Appl. Electrochem.* **2016**, *46*, 123–148. [CrossRef]
13. Scogings, A. Graphite: Where size matters. *Aust. Paydirt* **2015**, *1*, 78–79.
14. Dill, H.G.; Kus, J.; Goldmann, S.; Suárez-Ruiz, I.; Neumann, T.; Kaufhold, S. The physical-chemical regime of a sulfide-bearing semi-graphite mineral assemblage in metabasic rocks (SE Germany)—A multidisciplinary study of the missing link between impsonite and graphite. *Int. J. Coal Geol.* **2019**, *214*, 103262. [CrossRef]
15. Crespo, E.; Luque, F.J.; Barrenechea, J.F.; Rodas, M. Influence of grinding on graphite crystallinity from experimental and natural data: Implications for graphite thermometry and sample preparation. *Mineral. Mag.* **2006**, *70*, 697–707. [CrossRef]
16. Sandmann, D.; Haser, S.; Gutzmer, J. Characterisation of graphite by automated mineral liberation analysis. *Miner. Process. Extr. Metall.* **2014**, *123*, 184–189. [CrossRef]
17. Al-Ani, T.; Leinonen, S.; Ahtola, T.; Salvador, D. High-Grade Flake Graphite Deposits in Metamorphic Schist Belt, Central Finland—Mineralogy and Beneficiation of Graphite for Lithium-Ion Battery Applications. *Minerals* **2020**, *10*, 680. [CrossRef]
18. Spencer, S.; Sutherland, D. Stereological correction of mineral liberation grade distributions estimated by single sectioning of particles. *Image Anal. Stereol.* **2000**, *19*, 175–182. [CrossRef]
19. Kyle, J.R.; Ketcham, R.A. In situ distribution of gold in oes using high resolution X-ray computed tomography. *Econ. Geol.* **2003**, *98*, 1697–1701. [CrossRef]
20. Kyle, J.R.; Mote, A.S.; Ketcham, R.A. High resolution X-ray computed tomography studies of Grasberg porphyry Cu-Au ores, Papua, Indonesia. *Min. Depos.* **2008**, *43*, 519–532. [CrossRef]
21. Chisambi, J.; von der Heyden, B.P.; Tshibalanganda, M.; Le Roux, S.G. Gold Exploration in Two and Three Dimensions: Improved and Correlative Insights from Microscopy and X-Ray Computed Tomography. *Minerals* **2020**, *10*, 476. [CrossRef]

22. Dominy, S.C.; Platten, I.M.; Howard, I.E.; Elangovan, P.; Armstrong, R.; Minnitt, R.C.A.; Abel, R.L. Characterisation of gold ores by X-ray computed tomography—Part 2: Applications to the determination of gold particle size and distribution. In Proceedings of the 1st AusIMM International Geometallurgy Conference, Brisbane, Australia, 5–7 September 2011; pp. 293–309.
23. Ghorbani, Y.; Becker, M.; Petersen, J.; Morar, S.H.; Mainza, A.; Mainza, J.-P. Use of X-ray computed tomography to investigate crack distribution and mineral dissemination in sphalerite ore particles. *Miner. Eng.* **2011**, *24*, 1249–1257. [CrossRef]
24. Godel, B.; Barnes, S.J.; Barnes, S.-J.; Maier, W.D. Platinum ore in three dimensions: Insights from high-resolution X-ray computed tomography. *Geology* **2010**, *38*, 1127–1130. [CrossRef]
25. Godel, B. High-Resolution X-Ray Computed Tomography and Its Application to Ore Deposits: From Data Acquisition to Quantitative Three-Dimensional Measurements with Case Studies from Ni-Cu-PGE Deposits. *Econ. Geol.* **2013**, *108*, 2005–2019. [CrossRef]
26. Sittner, J.; Brovchenko, V.; Siddique, A.; Buyse, F.; Boone, M.; Renno, A.D.; Cnudde, V. Three-Dimensional Distribution of Platinum Group Minerals in Natural MSS-ISS Ores From the Norilsk One Deposit, Russia. *Front. Earth Sci.* **2022**, *10*. [CrossRef]
27. Le Roux, S.G.; Du Plessis, A.; Rozendaal, A. The quantitative analysis of tungsten ore using X-ray microCT: Case study. *Comput. Geosci.* **2015**, *85*, 75–80. [CrossRef]
28. Rozendaal, A.; Le Roux, S.G.; Du Plessis, A.; Philander, C. Grade and product quality control by microCT scanning of the world class Namakwa Sands Ti-Zr placer deposit West Coast, South Africa: An orientation study. *Miner. Eng.* **2017**, *116*, 152–162. [CrossRef]
29. Mees, F.; Swennen, R.; van Geet, M.; Jacobs, P. *Applications of X-Ray Computed Tomography in the Geosciences*; Geological Society: London, UK, 2003; ISBN 1862391394.
30. Jerram, D.A.; Mock, A.; Davis, G.R.; Field, M.; Brown, R.J. 3D crystal size distributions: A case study on quantifying olivine populations in kimberlites. *Lithos* **2009**, *112*, 223–235. [CrossRef]
31. Kyle, J.R.; Ketcham, R.A. Application of high resolution X-ray computed tomography to mineral deposit origin, evaluation, and processing. *Ore Geol. Rev.* **2015**, *65*, 821–839. [CrossRef]
32. Jerram, D.A.; Higgins, M.D. 3D Analysis of Rock Textures: Quantifying Igneous Microstructures. *Elements* **2007**, *3*, 239–245. [CrossRef]
33. Gualda, G.A.R.; Rivers, M. Quantitative 3D petrography using x-ray tomography: Application to Bishop Tuff pumice clasts. *J. Volcanol. Geotherm. Res.* **2006**, *154*, 48–62. [CrossRef]
34. Vásrhelyi, L.; Kónya, Z.; Kukovecz, Á.; Vajtai, R. Microcomputed tomography-based characterization of advanced materials: A review. *Mater. Today Adv.* **2020**, *8*, 100084. [CrossRef]
35. Cnudde, V.; Boone, M.N. High-resolution X-ray computed tomography in geosciences: A review of the current technology and applications. *Earth-Sci. Rev.* **2013**, *123*, 1–17. [CrossRef]
36. Berger, M.J.; Hubbell, J.H.; Seltzer, S.M.; Chang, J.; Coursey, J.S.; Sukumar, R.; Zucker, D.S.; Olsen, K. X-COM: Photon Cross Sections Database. Available online: http://physics.nist.gov/PhysRefData/Xcom/Text/XCOM (accessed on 5 December 2022).
37. van Grieken, R.; Markowicz, A. *Handbook of X-Ray Spectrometry*; CRC Press: Boca Raton, FL, USA, 2001; ISBN 9780203908709.
38. Hsieh, J. *Computed Tomography: Principles, Design, Artifacts, and Recent Advances*; SPIE Press: Bellingham, WA, USA, 2003; ISBN 9780819444257.
39. Ketcham, R.A.; Carlson, W.D. Acquisition, optimization and interpretation of X-ray computed tomographic imagery: Applications to the geosciences. *Comput. Geosci.* **2001**, *27*, 381–400. [CrossRef]
40. Volume Graphics GmbH. *VGSTUDIO MAX 3.5*; Volume Graphics GmbH: Heidelberg, Germany, 2021.
41. Object Research Systems. *Dragonfly*; Object Research Systems: Montreal, QC, Canada, 2021.
42. Zhou, Z.-H. *Machine Learning*; Springer Nature: Berlin/Heidelberg, Germany, 2021; ISBN 9789811519673.
43. Li, X.; Zhang, G.; Li, K.; Zheng, W. Deep Learning and Its Parallelization. In *Big Data: Principles and Paradigms*; Buyya, R., Calheiros, R.N., Dastjerdi, A.V., Eds.; Elsevier: Cambridge, MA, USA; Morgan Kaufmann: Burlington, MA, USA, 2016; pp. 95–118. ISBN 978-0-12-805394-2.
44. Breiman, L. Random Forests. *Mach. Learn.* **2001**, *45*, 5–32. [CrossRef]
45. Ronneberger, O.; Fischer, P.; Brox, T. U-Net: Convolutional Networks for Biomedical Image Segmentation. In Proceedings of the International Conference on Medical image computing and computer-assisted intervention, Munich, Germany, 5–9 October 2015; pp. 234–241.
46. Novikov, A.; Major, D.; Wimmer, M.; Lenis, D.; Bühler, K. Deep Sequential Segmentation of Organs in Volumetric Medical Scans. *IEEE Trans. Med. Imaging* **2019**, *38*, 1207–1215. [CrossRef]
47. Ren, Y.; Li, J.; Sun, X.; Li, Z.; Sun, Z. Genesis of Metal Sulfides and Its Significance on Graphite Mineralization in the Huangyangshan Graphite Deposit, East Junggar, Xinjiang Province, China. *Minerals* **2022**, *12*, 1450. [CrossRef]
48. Fatima, A.; Venkatesh, A.S.; Mukherjee, R.; Agrawal, A.K.; Singh, B.; Sarkar, P.S.; Kashyap, Y.; Shripathi, T. 3D spatial distribution of ore mineral phases using high resolution synchrotron micro-computed tomography (μCT) combined with optical microscopy. *Appl. Radiat. Isot.* **2019**, *148*, 49–59. [CrossRef]
49. Jara, A.D.; Woldetinsae, G.; Betemariam, A.; Kim, J.Y. Mineralogical and petrographic analysis on the flake graphite ore from Saba Boru area in Ethiopia. *Int. J. Min. Sci. Technol.* **2020**, *30*, 715–721. [CrossRef]
50. Zhang, X.; Zhang, L.Y.; Qiu, Y.S.; Qu, X. Beneficiation of a Low-Grade Flaky Graphite Ore from Australia by Flotation. *AMR* **2015**, *1090*, 188–192. [CrossRef]

51. Mitchell, C.J. *Industrial Minerals Laboratory Manual: Flake Graphite*; Technical Report WG/92/30; British Geological Survey: Nottingham, UK, 1993; p. 31.
52. Kim, B.G.; Choi, S.K.; Park, C.L.; Chung, H.S.U.N.; Jeon, H.S.O. Inclusion of Gangue Mineral and Its Mechanical Separation from Expanded Graphite. *Part. Sci. Technol.* **2003**, *21*, 341–351. [CrossRef]
53. Hanna, R.D.; Ketcham, R.A. X-ray computed tomography of planetary materials: A primer and review of recent studies. *Geochemistry* **2017**, *77*, 547–572. [CrossRef]
54. Ketcham, R.A. Accurate three-dimensional measurements of features in geological materials from X-ray computed tomography data. In *Advances in X-ray Tomography for Geomaterials*; Desrues, J., Viggiani, G., Bésuelle, P., Eds.; ISTE: London, UK, 2006; pp. 143–148.

**Disclaimer/Publisher's Note:** The statements, opinions and data contained in all publications are solely those of the individual author(s) and contributor(s) and not of MDPI and/or the editor(s). MDPI and/or the editor(s) disclaim responsibility for any injury to people or property resulting from any ideas, methods, instructions or products referred to in the content.